

Trajectory Design of a Rocket–Scramjet–Rocket Multistage Launch System

1

Sholto O. Forbes-Spyratos,^{*} Michael P. Kearney,[†] Michael K. Smart,[‡] and Ingo H. Jahn[§]
University of Queensland, Brisbane, Queensland 4072, Australia

DOI: 10.2514/1.A34107

The integration of a reusable scramjet vehicle as the second stage of a multistage space launch system has the potential to reduce the cost of small-payload orbital launches. This paper determines the maximum payload to orbit trajectory of a multistage rocket–scramjet–rocket system. This trajectory is calculated by formulating the problem as an optimal control problem, and then solving it using the pseudospectral method. Using this method, it is determined that the optimal trajectory for the scramjet stage involves an initial decrease in dynamic pressure, followed by constant-dynamic-pressure flight, and finally a pullup maneuver. This optimal trajectory results in an 8.35% improvement in payload mass to orbit when compared to a constant-dynamic-pressure trajectory with minimum pullup. Furthermore, the optimal pullup maneuver decreases the maximum dynamic pressure experienced by the final rocket stage by 20.3%. The sensitivity of the trajectory is tested by varying the maximum allowable dynamic pressure and the drag produced by the vehicle. A maximum dynamic pressure variation of ± 5 kPa is shown to produce only +3.8% and –3.5% variations in the payload mass. A drag increase of 10% is shown to produce a similar optimal trajectory shape, indicating robustness with variation of the vehicle aerodynamics.

Nomenclature

A	=	reference area, m ²
a	=	acceleration, m/s ²
C	=	cost functional
C_L, C_D	=	aerodynamic coefficients
D	=	drag, N
F	=	force, N
g_0	=	gravitational acceleration at Earth's surface, m/s ²
I_{sp}	=	specific impulse, s
L	=	lift, N
M	=	end point cost functional
m	=	mass, kg
P	=	integrated cost functional
q	=	dynamic pressure, Pa
r	=	radius from Earth center, m
T	=	thrust, N
t	=	time, s
\mathbf{u}	=	control variables
v	=	velocity, m/s
\mathbf{x}	=	state variables
w_{cap}	=	capture width
α	=	angle of attack, rad
γ	=	flight-path angle, rad
ζ	=	heading angle, rad
λ	=	inequality constraint functional
ξ	=	longitude, rad
ρ	=	density, kg/m ³
ϕ	=	latitude, rad
ψ	=	equality constraint functional

ω = angular velocity, rad/s

Subscripts

AoA	=	angle of attack
a, b	=	nominal stage numbers
atm	=	atmospheric
E	=	earth
e	=	exit
f	=	final
LEO	=	low Earth orbit
LH2	=	liquid hydrogen
LOX	=	liquid oxygen
SL	=	sea level
vac	=	vacuum
0	=	initial
1	=	first-stage rocket
2	=	second-stage scramjet vehicle
3	=	third-stage rocket
→	=	stage transition

I. Introduction

CURRENTLY, most small satellites comanifest with a larger payload, leaving their launch schedule and trajectory at the mercy of the major payload. The increasing demand for small satellite launches [1] is driving the development of cheap and efficient launch systems for independent launches of small satellites into tailored orbits on a fast schedule. A multistage launch system incorporating a scramjet second stage has been proposed as a dedicated small satellite launch vehicle [2]. Scramjets (supersonic combustion ramjets) are airbreathing engines that operate over Mach numbers in the hypersonic range [3]. Scramjet engines are a primary candidate for powering the next generation of small payload launch vehicles, producing higher specific impulse I_{sp} than rockets within their operating range. Other benefits of scramjets include increased flexibility of launch windows and an increased range of mission capabilities [4]. Scramjets can accelerate a launch vehicle without the need to carry oxidizer on board, providing mass savings as compared to rocket-powered vehicles. The reduction of mass carried within the vehicle fuselage enables the integration of avionics and landing gear, allowing for the design of a reusable vehicle in the style of conventional aerospace vehicles. However, a scramjet-incorporating launch system requires two rocket stages: a first-stage rocket capable of accelerating the scramjet vehicle to its operating speed, and a final rocket stage for placing the payload in orbit.

Presented as Paper 2017 at the 21st AIAA International Space Planes and Hypersonics Technologies Conference, Xiamen, China, 6–9 March 2017; received 3 October 2017; revision received 3 May 2018; accepted for publication 15 June 2018; published online XX epubMonth XXXX. Copyright © 2018 by the American Institute of Aeronautics and Astronautics, Inc. All rights reserved. All requests for copying and permission to reprint should be submitted to CCC at www.copyright.com; employ the ISSN 0022-4650 (print) or 1533-6794 (online) to initiate your request. See also AIAA Rights and Permissions www.aiaa.org/randp.

^{*}Ph.D. Candidate, Centre for Hypersonics, School of Mechanical and Mining Engineering, Member AIAA.

[†]Lecturer, School of Mechanical and Mining Engineering.

[‡]Professor, Centre for Hypersonics, School of Mechanical and Mining Engineering, Senior Member AIAA.

[§]Lecturer, Centre for Hypersonics, School of Mechanical and Mining Engineering, Member AIAA.

This paper presents a trajectory designed using optimal control methods for a rocket–scramjet–rocket small satellite launch system proposed by the Centre for Hypersonics at the University of Queensland [5], incorporating the scramjet-powered accelerator for reusable technology advancement (SPARTAN) scramjet accelerator. The trajectory profile of this rocket–scramjet–rocket system has previously been designed around the scramjet stage flying a constant-dynamic-pressure trajectory [5], which is in line with similar multistage vehicles [6,7]. A constant-dynamic-pressure trajectory follows the maximum dynamic pressure that the scramjet-powered vehicle is able to withstand structurally, ensuring maximum thrust production from the scramjet engines. However, flying a maximum dynamic pressure trajectory also results in the release of the third-stage rocket into a high dynamic pressure at a low flight-path angle.

Previously, when flying a constant-dynamic-pressure scramjet-stage trajectory, the Pratt and Whitney RL-10A-3A pumped engine was used as the propulsion system for the third-stage rocket [5]. This study instead uses a modified SpaceX Kestrel engine [8]. This is more cost efficient than the RL-10-3A, with the tradeoff of lower thrust and efficiency. Due to the reduced thrust, the Kestrel powered third stage is unable to reach orbit if released from a near-horizontal flight at maximum dynamic pressure. Instead, a minimal pullup is required to release the third stage at a lower dynamic pressure.

A trajectory with the minimum required pullup produces maximum acceleration from the scramjet stage by maximizing the dynamic pressure during flight. However, a minimum pullup trajectory may not be optimal for the overall multistage system. For example, a minimum pullup trajectory may still release the final stage into a high dynamic pressure environment at a potentially suboptimal flight-path angle. This release point may result in suboptimal performance of the final-stage rocket and the inclusion of unnecessary design constraints. A larger pullup may produce an overall favorable tradeoff by allowing for the scramjet stage to be used to increase the altitude and flight-path angle of the launch vehicle, enabling the final-stage rocket to operate with reduced drag. However, as the altitude increases, the thrust of the airbreathing engine is reduced, due to a lower mass flow rate into the engine.

In previous studies, the optimized trajectories for launch vehicles using rocket and airbreathing propulsion within a single stage have been shown to exhibit flight at maximum dynamic pressure for the majority of the airbreathing operation, followed by a pullup before airbreathing engine cutoff [9–15]. A trajectory involving a pullup has been shown to be the optimal trajectory for vehicles in which the rocket engines are not ignited until circularization altitude [9,10], vehicles in which the rocket engine is ignited immediately after airbreathing engine cutoff [11–13], as well as for vehicles that operate in a combined scramjet–rocket mode [14,15].

For launch systems with airbreathing and rocket propulsion combined within a single stage, an optimized pullup maneuver is a simple tradeoff between velocity and altitude. However, for the proposed scramjet–rocket multistage system, the scramjet stage and rocket stage are sequential and completely separate. The resultant change in mass and aerodynamic characteristics adds to the complexity of the trajectory analysis. For a robust multistage trajectory design, there is a tradeoff between 1) the high efficiency of the scramjet engines, 2) the thrust produced by the scramjet engines, 3) the potential thrust of the rocket engines after separation, 4) the energy necessary to increase the altitude of the scramjet stage, and 5) the aerodynamic efficiency when performing the required direction change.

A pullup maneuver has previously been identified as having potential advantages for multistage airbreathing-rocket systems [16–18]. However, these pullup maneuvers were minimum pullups imposed by rocket flight constraints [16,17] or were prescribed in a suboptimal trajectory with variations in dynamic pressure [18]. The inherent intricacies of a multistage, partially airbreathing system (particularly, the complexity of transition between the airbreathing and rocket stages) necessitates an investigation into the optimal launch trajectory design.

This paper uses an optimal control theory to generate the optimal trajectory path for a rocket–scramjet–rocket multistage vehicle. Optimal control theory allows a trajectory to be optimized in its

entirety and has been widely used in aerospace applications for computing trajectories when there is a global objective to be optimized, such as minimum fuel [19–21] or maximum crossrange [22–24]. Prescribing a trajectory to produce an optimal result (using a defined flight path or targeted controller) requires the optimal trajectory conditions to be known a priori. Optimal control allows for the calculation of a flight path that optimizes the end goal while satisfying all vehicle constraints from few initial assumptions [25].

Highly nonlinear control problems (such as a complex model of hypersonic flight) necessitate the use of direct methods such as direct single shooting, multiple shooting, or collocation [25]. Direct methods discretize the trajectory optimization problem and solve the nonlinear programming (NLP) problem that results computationally [26,27]. This solution is calculated using an NLP solving technique such as sequential quadratic programming (SQP), which is widely used for trajectory optimization due to its high efficacy [25,28]. The most powerful methods of optimal control are arguably direct collocation methods, in which the state and control variables are approximated using specified basis functions of splines or polynomials [25,26,29]. The use of global orthogonal polynomials as basis functions, collocated at nodes obtained from a Gaussian quadrature, is referred to as the pseudospectral method, due to the resultant accuracy of the problem converging spectrally (at an exponential rate) as the number of collocation nodes increases [25,30]. The use of the spectral method ensures that higher-order terms of the dynamic equations are solved, and it facilitates solutions with high accuracy, even with relatively few collocation points [31]. The pseudospectral method is used in this study due to its accuracy, efficiency, and radius of convergence when compared to other optimal control techniques [26,29]. The accuracy and validity of this method have been demonstrated for a variety of aerospace applications [19,20,32,33].

The remainder of the paper is as follows: Section II presents the design characteristics of all three stages. Section III presents the aerodynamic modeling of the system. Section IV presents an overview of the optimal control theory used, including the problem definition and a description of the pseudospectral method. Section V presents optimal trajectory results for all three stages, including results verifying the use of the pseudospectral method, optimal trajectory results for a range of maximum dynamic pressure conditions, and optimal trajectory results with variations in the vehicle's aerodynamic characteristics.

II. SPARTAN System

The system to be optimized, shown in Figs. 1 and 2, includes a rocket-powered first stage, a scramjet-powered second stage, and a rocket-powered third stage for payload delivery to heliosynchronous orbit. The SPARTAN system [5,34,35] is used in this study as a representative model for future multistage access to space systems, incorporating airbreathing second stages. The following section details the design characteristics of all three stages.

A. First-Stage Rocket

The first-stage rocket is required to deliver the second stage to near horizontal flight at Mach 5.1 flight conditions; after which, it is discarded. To achieve this, the first-stage rocket is modeled as a Falcon-1e first stage scaled down lengthwise to 9.5 m, keeping the original diameter of 1.67 m [8]. The first stage is attached to the rear of

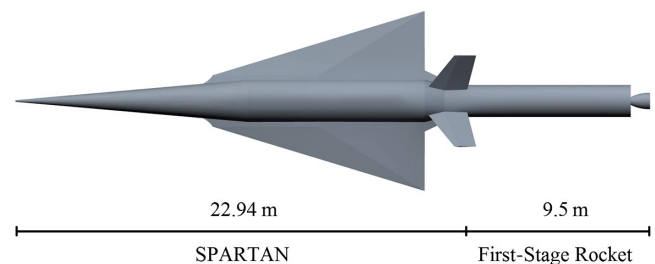


Fig. 1 Model of the first-stage rocket and scramjet vehicle.



Fig. 2 Side view of all three stages, including internal view.

the scramjet second stage and is powered by a single liquid oxygen (LOX)–kerosene Merlin 1-C engine. This first stage has a structural mass of 1356 kg, which is determined by scaling of the structural mass of the Falcon-1e. The engine mass is kept constant. The mass of the fuel in the first stage is scaled as part of the optimization routine because the dynamics of the vehicle and its ability to reach a given separation point are very closely coupled to the available fuel mass.

B. Scramjet Accelerator

The scramjet-powered accelerator for reusable technology advancement is a scramjet-powered accelerator under development by the University of Queensland, which is to be used as the second stage in a scramjet–rocket-powered system for delivering small payloads to heliosynchronous orbit [5]. The SPARTAN is designed to be capable of flying back after separation to a designated airfield close to the launch site.

The SPARTAN has a fuselage diameter of 2.1 m and a mass of 9819 kg, including the third-stage rocket. It has been sized to hold the third-stage rocket within the fuselage to reduce aerodynamic drag, as shown in Fig. 2. The SPARTAN has three fuel tanks, two cylindrical tanks housed below the third-stage rocket, and one conical tank housed in the nose of the vehicle. These tanks have a total volume of 22.0 m³ and a total liquid hydrogen (LH2) storage capacity of 1562 kg. The SPARTAN is powered by four scramjet engines located on the bottom portion of the fuselage, sized to a nominal capture width of 0.65 m. These engines are based on the rectangular-to-elliptical shape transition (REST) scramjet engine design [36], with modified inlets to fit to a conical fuselage via a C-REST inlet configuration [37]. Previous studies have indicated that using the SPARTAN as part of a three-stage access to a space system can produce payload mass fractions that compare favorably with similarly sized rocket systems [5,34].

C. Third-Stage Rocket

The third-stage rocket is initially housed within the SPARTAN fuselage, as shown in Fig. 2. After separation from the SPARTAN, the third-stage rocket initiates a burn and performs an altitude-increasing maneuver. At the end of the initial burn, the third-stage rocket is allowed to coast until reaching apogee; at which point, it must have an altitude of at least 100 km to ensure that the rocket is in an exoatmospheric orbit. The orbit is circularized using a further short burn; after which, the payload delivery to heliosynchronous orbit is completed using a Hohmann transfer. The payload to orbit is determined by calculating the mass of the vehicle at the end of the Hohmann transfer. The structural mass is removed, and the remaining mass is taken to be the payload-to-orbit capability of the vehicle.

The third-stage rocket (Fig. 3) has a total length of 9 m, a diameter of 1.1 m, and a total initial mass of 3300 kg. It is modeled to be powered by a modified SpaceX LOX–kerosene Kestrel engine [8] weighing 52 kg. Previous studies used a LOX–LH2 upper stage based on the RL-10-3A engine [5]. In this study, the pressure-fed Kestrel engine is used rather than the pumped RL-10-3A to reduce the cost of the disposable third-stage rocket. The third stage has a structural mass of 285.7 kg, which is equivalent to a structural mass fraction of 0.09 (calculated without heat shield) and similar to the

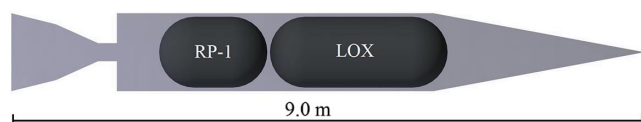


Fig. 3 Schematic of the third-stage rocket.

Falcon-1e second stage [8]. The in-atmosphere high-dynamic-pressure separation of the rocket stage requires the use of a heat shield that envelopes the rocket stage. The heat shield is constructed from a tungsten nose piece, a carbon–carbon cone, and a phenolic cork cylinder. The heat shield weighs 130.9 kg in total, and it is discarded when the rocket reaches a dynamic pressure of 10 Pa (atmospheric heating is assumed to be negligible at this point) [5,34].

III. Aerodynamics, Propulsion, and Dynamic Modeling

Multiple analysis tools are used to model the aerodynamics and propulsion of the stages of the SPARTAN system. These have been chosen based on appropriateness for the design and Mach number regime of each stage.

A. Aerodynamics

An aerodynamic database of the first-stage stack is generated using CART3D [38], which is a high-fidelity inviscid analysis computational fluid dynamics (CFD) package with adjoint-based mesh refinement. The CART3D package uses a Cartesian cut-cell approach [39], resulting in a mesh of cubes everywhere except at body-intersecting cells. CART3D is used to analyze the first-stage stack due to its applicability over a wide range of Mach numbers. CART3D has been used successfully in a variety of aerospace applications, including hypersonic launch systems [40], and has shown fair agreement when compared to experimental results for winged boosters at hypersonic speeds [41], as well as for supersonic missiles [42] and aircraft [43]. For the simulation, the vehicle geometry is created using Creo Parametric 3.0 software [44], and a body-fitted triangular mesh is generated using Pointwise 18.0 [45]. A pressure field for a Mach 2, -1° deg angle of attack (AOA) calculated using CART3D is shown in Fig. 4. Figure 5 shows an example of the

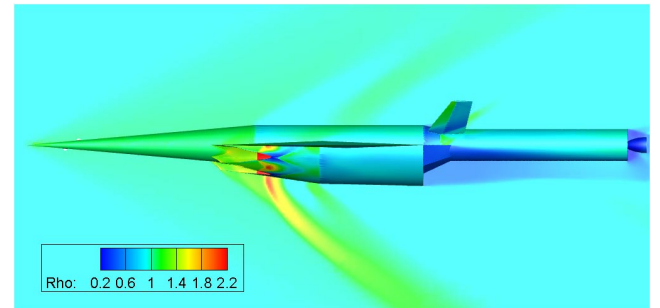


Fig. 4 Normalized density contours of first-stage flight with Mach 2 and -1° deg angle of attack.

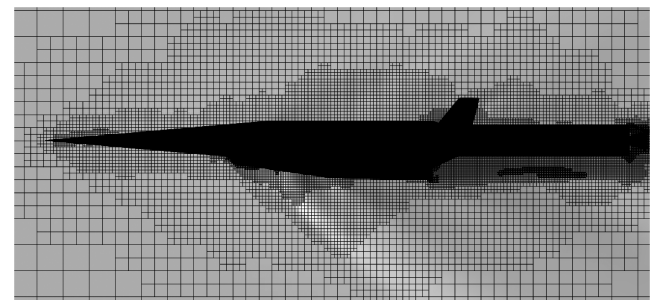


Fig. 5 Adaptive mesh generated close to vehicle by CART3D for Mach 2, -1° deg angle-of-attack flight conditions.

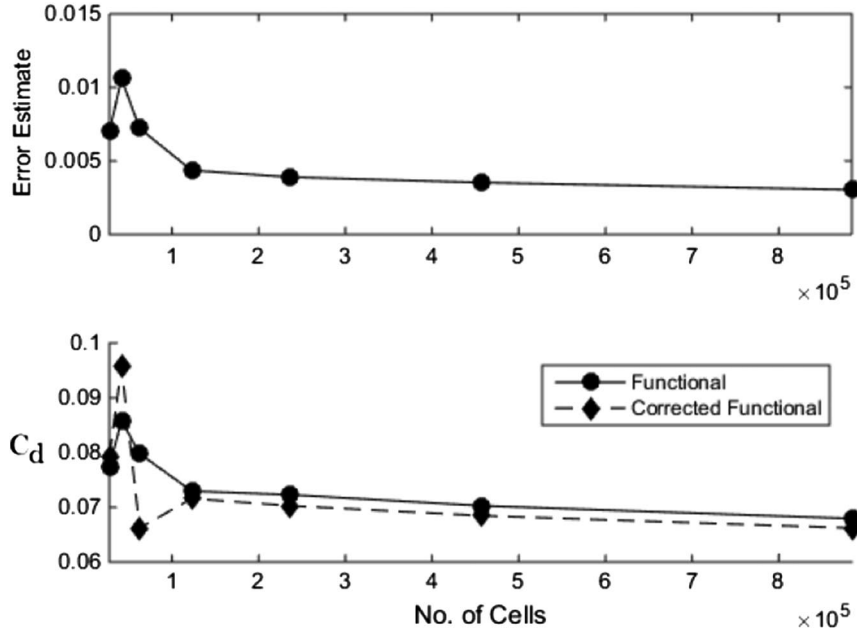


Fig. 6 CART3D verification parameters of error estimate and C_d functional.

mesh produced by CART3D. This mesh extends out to 50 body lengths at the far-field boundaries. Figure 6 examines convergence parameters of the CFD solution: the functional, its adjoint-based correction, and its error estimate. The functional and corrected functional converge and error estimates decrease steadily as the mesh is refined, indicating mesh convergence.

5 The aerodynamics of the SPARTAN second stage are simulated using a set of aerodynamic coefficients developed in HYPAERO [5,46]. HYPAERO produces aerodynamics for hypersonic vehicles using longitudinal strip theory to solve the surface pressures acting on the vehicle and to provide aerodynamic coefficients over the operating range of Mach numbers, angles of attack, and flap deflection angles of the vehicle. The flaps are used to trim the SPARTAN throughout its trajectory.

6 The aerodynamics of the third-stage rocket are determined using a database generated using Missile DATCOM [47], which is a preliminary design tool for estimating the aerodynamic characteristics of missile configurations. To limit the aerodynamic forces on the rocket, the maximum normal force allowable by the rocket structure is set as the normal force produced by a 10 deg angle of attack at 50 kPa flight. The maximum angle of attack of the third-stage rocket is thus limited to 10 deg at 50 kPa, and it is increased with altitude so that the maximum allowable normal force F_N is kept constant. Thrust vectoring is used to trim the third-stage rocket. The maximum thrust vector angle is limited to eight, which is similar to other small-sized pressure-fed rocket engines [48].

Atmospheric properties are drawn from the U.S. Standard Atmosphere 1976 [49].

B. Propulsion

The first-stage Merlin 1-C is modeled by scaling the sea-level thrust using the standard rocket thrust equation

$$T = T_{SL} + (P_{SL} - P_{atm})A_e \quad (1)$$

where T_{SL} is the sea level thrust; A_e is the exit area of 0.55 m²; and P_{SL} and P_{atm} are the atmospheric pressure at sea level and at the current flight altitude, respectively. The Merlin 1-C is throttled to a constant 85% of maximum thrust to enable the rocket to pitch easily, giving a sea level thrust of 472.5 kN [8]. The vacuum specific impulse is 304 s [8].

The scramjet engine model used is based on the C-REST database [5], which provides data points of engine performance over inlet conditions within the operational range, at 50 kPa dynamic pressure

equivalent conditions. These data are interpolated for the given inlet conditions to calculate the exit conditions and the specific impulse produced by the engine. The thrust T is then obtained by inclusion of the mass flow rate \dot{m} obtained via the inlet conditions, i.e., $T = g_0 \dot{m} I_{sp}$. The C-REST engine is a fixed geometry engine, which is designed for operability at high Mach numbers [5]. At lower Mach numbers, the addition of excessive fuel may cause the engine to choke and unstart, resulting in total loss of thrust [5]. To avoid unstart, an equivalence ratio of less than one is set at low Mach numbers.

The third-stage Kestrel engine was modified to provide 50% increased thrust over the standard Kestrel engine. This has been modeled by increasing the mass flow rate and nozzle throat diameter, although the nozzle exit diameter has not been changed. This results in the nozzle area ratio decreased from 60 [8] to 40, lowering the vacuum efficiency by 2% [50]. The modified third-stage Kestrel engine had a vacuum specific impulse of 310.7 s [8] and a vacuum thrust of 45.1 kN. The thrust is modeled using the standard rocket thrust equation to scale for atmospheric pressure:

$$T = T_{vac} - P_{atm}A_e \quad (2)$$

C. Dynamic Model

The drag and lift produced by each stage of the vehicle are calculated using the standard definition of the aerodynamic coefficients:

$$D = \frac{1}{2} \rho C_D v^2 A \quad (3)$$

$$L = \frac{1}{2} \rho C_L v^2 A \quad (4)$$

The dynamics of all stages are calculated using an geodetic rotational reference frame, written in terms of the radius from the center of the Earth r , the longitude ξ , the latitude ϕ , the flight-path angle γ , the velocity v , and the heading angle ζ . Roll and yaw angles are constrained to 0 deg. The equations of motion are as follows [20]:

$$\dot{r} = v \sin \gamma \quad (5)$$

$$\dot{\xi} = \frac{v \cos \gamma \cos \zeta}{r \cos \phi} \quad (6)$$

$$\dot{\phi} = \frac{v \cos \gamma \sin \zeta}{r} \quad (7)$$

$$\dot{\gamma} = \frac{T \sin \alpha}{mv} + \left(\frac{v}{r} - \frac{\mu_E}{r^2 v} \right) \cos \gamma + \frac{L}{mv} + \cos \phi \left[2\omega_E \cos \zeta + \frac{\omega_E^2 r}{v} (\cos \phi \cos \gamma + \sin \phi \sin \gamma \sin \zeta) \right] \quad (8)$$

$$\dot{v} = \frac{T \cos \alpha}{m} - \frac{\mu_E}{r^2} \sin \gamma - \frac{D}{m} + \omega_E^2 r \cos \phi (\cos \phi \sin \gamma - \sin \phi \cos \gamma \sin \zeta) \quad (9)$$

$$\dot{\zeta} = -\frac{v}{r} \tan \phi \cos \gamma \cos \zeta + 2\omega_E \cos \phi \tan \gamma \sin \zeta - \frac{\omega_E^2 r}{v \cos \gamma} \sin \phi \cos \phi \cos \zeta - 2\omega_E \sin \phi \quad (10)$$

IV. Trajectory Optimization

The three-stage trajectory of the launch vehicle forms a complex optimization problem, spanning a large range of velocity and altitude conditions with multiple changes in the vehicle dynamics and propulsion method. To simplify the problem, the three stages are calculated separately and coupled together at the separation points $\mathbf{x}_1(t_{1,f})$ (first to second stages) and $\mathbf{x}_2(t_{2,f})$ (second to third stages). Together, these problems have the form of a sequential decision-making problem in which the global optimal solution can be determined using dynamic programming [51].

A. Trajectory Planning as an Optimal Control Problem

The optimal trajectory for each stage is found by determining the control function $\mathbf{u}_a(t)$ that minimizes the objective function:

$$\min_{\mathbf{u}_a} C_a(\mathbf{x}_a(t_a), \mathbf{u}_a(t_a)) + C_{a \rightarrow b}(\mathbf{x}_a(t_{a,f})) \quad (11)$$

where a is the vehicle stage to be optimized, and b is the following stage. $C_a(\mathbf{x}_a(t_a), \mathbf{u}_a(t_a))$ is a continuous cost function and $C_{a \rightarrow b}$ is a terminal cost, dependent on the state variables $\mathbf{x}_a(t_{a,f})$ at the end of the stage trajectory. This terminal cost is used in this study to connect the optimal control problem to the next stage, which allows for the overall trajectory to be designed using dynamic programming. The optimization of Eq. (11), subject to the vehicle dynamics, has the form of a Bolza optimization problem, in which an objective function $J(\mathbf{x}, \mathbf{u}, t_f)$ is minimized:

$$J(\mathbf{x}(t), \mathbf{u}(t)) = \underbrace{M[\mathbf{x}(t_f)]}_{C_{a \rightarrow b}(\mathbf{x}_a(t_{a,f}))} + \underbrace{\int_{t_0}^{t_f} P[\mathbf{x}(t), \mathbf{u}(t)] dt}_{C_a(\mathbf{x}_a(t_a), \mathbf{u}_a(t_a))}, \quad t \in [t_0, t_f] \quad (12)$$

where M is the terminal cost function, and P is the stage cost. The optimization problem is subject to a set of state dynamics $\dot{\mathbf{x}}(t)$ that describe the behavior of the system over the solution space:

$$\dot{\mathbf{x}}_a(t_a) = f[t_a, \mathbf{x}_a(t_a), \mathbf{u}_a(t_a)] \quad (13)$$

These state dynamics correspond to the equations of motion of the vehicle, as defined in Sec. III.C. The optimization problem is constrained by the boundary conditions of the system at the initial and final time points:

$$\boldsymbol{\psi}_0[\mathbf{x}_a(t_{a,0}), t_{a,0}] = \mathbf{0} \quad (14)$$

$$\boldsymbol{\psi}_f[\mathbf{x}_a(t_{a,f}), t_{a,f}] = \mathbf{0} \quad (15)$$

as well as a set of inequality constraints defining the bounds of the problem:

$$\boldsymbol{\lambda}[\mathbf{x}_a(t_a), \mathbf{u}_a(t_a)] \leq \mathbf{0} \quad (16)$$

These inequality constraints are chosen to span the possible operating range of the vehicle to ensure an optimal solution. Solving this Bolza problem in a discrete simulation requires the use of numerical solution methods. The first- and second-stage trajectory solutions use the pseudospectral method, which is a form of direct spectral collocation [25,26]. To perform this optimization, the pseudospectral method solver DIDO was chosen [52].

The third-stage trajectory optimization is performed using the direct single shooting method [53]. The direct single shooting method is selected for the third-stage trajectory optimization due to its ease of initialization, allowing it to automatically solve repeated instances of the problem with different initial conditions. The direct single shooting method uses an SQP algorithm to directly solve for the optimal time-discretized control history [25]. This control history is optimized subject to the dynamics, cost, and constraints of the system, which are evaluated at each iteration using forward simulation. Due to the strong dependence on the control history, the direct single shooting method is highly sensitive to the initial guess for nonlinear problems, and it is mostly suited to solving well-conditioned problems.

B. Optimization Methodology

The program LODESTAR (which stands for launch optimization and data evaluation for scramjet trajectory analysis research) has been developed to produce an optimal trajectory path for a rocket–scramjet–rocket launch vehicle. LODESTAR provides subroutines that enable the simulation of rocket and scramjet vehicles in 6 deg of freedom and is designed specifically for use within an optimization routine, including aerodynamic and engine performance calculations as well as trim analysis. LODESTAR also adaptively provides bound and guess inputs to the optimization routines. In this study, LODESTAR uses a direct single shooting method for the third stage; and DIDO [52,54], which is a proprietary pseudospectral method optimization package, uses a direct single shooting method for the first and second stages. DIDO solves the optimization problem at shifted Legendre–Gauss–Lobatto points using a spectral algorithm based on an active-set method within SNOPT, which is an SQP solver [52,55].

The three stages are considered as separate optimization problems, which are coupled at the stage separation points. The first and second stages are coupled by a separation point that is determined by the optimal altitude and flight-path angle for the second-stage trajectory, as well as the minimum starting velocity of the scramjet. This separation point is used as an end condition on the first-stage optimization. For the minimum pullup case, the second and third stages are coupled by the end point of the second-stage simulation, which is reached when the second stage has expended all of its fuel. The third-stage trajectory is optimized for maximum payload from the end of the second-stage trajectory.

For the maximum payload cases, the second and third stages are coupled a priori by running the third-stage optimization repeatedly for different separation altitudes, velocities, and angles; and tabulating the results. The terminal cost of the payload to orbit, for the second-stage optimization, is generated from this table using interpolation. By setting the objective of the third-stage optimization to a maximize payload mass, the coupled optimization of the second stage in turn maximizes the payload mass over both stages. The coupling of the stage simulations means that the stage optimizations are performed backward in time to design the complete trajectory: first, the third stage is optimized for a maximum payload to orbit and is tabulated over a range of altitudes, velocities, and flight-path angles; then, the second stage is optimized for the maximum payload to orbit; and, lastly, the first stage is optimized for the fuel mass to reach the optimal second-stage start point.

1. Third-Stage Optimization

The third-stage rocket trajectory is optimized for the maximum payload to orbit, so that the second-stage scramjet and third-stage rocket form a Bolza optimization problem and maximize the payload collectively. The cost function is configured to maximize the payload at the end of the trajectory:

$$\min_{u_3} C_{3 \rightarrow \text{LEO}}(\mathbf{x}_3(t_{3,f})) \quad (17)$$

where

$$C_{3 \rightarrow \text{LEO}}(\mathbf{x}_3(t_{3,f})) = -m_{\text{payload}} \quad (18)$$

and $\mathbf{x}_3(t_{3,f})$ are the tabulated separation conditions of the altitude, velocity, and flight-path angle. A direct shooting optimization is performed with 20 angle-of-attack node points, which are interconnected by spline interpolation from separation $t_{3,0}$ to a variable end time $t_{\text{AoA},f}$. At this time, the angle of attack is gradually reduced so that it reaches zero at the end of the burn time $t_{\text{burn},f}$, which is also variable. A constraint is imposed so that the angle of attack must have at least 10 s to reduce to zero at the end of the burn (i.e., $t_{\text{burn},f} - t_{\text{AoA},f} \geq 10$) to allow time for maneuvering.

The payload mass is calculated after the Hohmann transfer to the desired orbit, taking the remaining fuel to be the effective payload capacity. SQP is used to find the optimal solution using MATLAB's `fmincon` solver [56]. As an example, the tabulated optimal payload-to-orbit results for a 2875 m/s third-stage release velocity are shown in Fig. 7. The payload increases with both the altitude and release angle; however, it is clear that the potential payload increase due to increasing the separation altitude lessens as the release angle increases.

2. Second-Stage Optimization: Constant Dynamic Pressure, Minimum Pullup

The constant-dynamic-pressure case with minimum pullup optimizes the trajectory to minimize variation from the desired dynamic pressure, with the third-stage release angle constrained to 1.5 deg, which is approximately the minimum release angle necessary to reach orbit. This constraint results in a trajectory with the smallest possible pullup maneuver. The trajectory is configured with a quadratic cost function centered around a 50 kPa dynamic pressure:

$$\min_{u_2} C_2(\mathbf{x}_2(t_2), \mathbf{u}_2(t_2)) \quad (19)$$

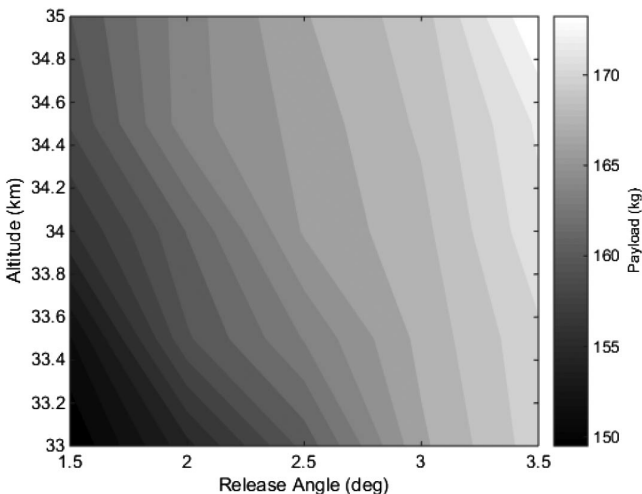


Fig. 7 Payload mass results with variation in rocket-stage release point for $v = 2875$ m/s, with a heading angle of 1.78 rad and a latitude of -0.136 rad.

where

$$C_2(\mathbf{x}_2(t_2), \mathbf{u}_2(t_2)) = \int_{t_{2,0}}^{t_{2,f}} \frac{(q - 50 \times 10^3)^2 + 10^5}{10^5} dt \quad (20)$$

This quadratic function provides a smooth, continuous function to increase solver stability and ensure uniform dynamic pressure. Scaling and translating constants of 10^5 are included to normalize the cost function in order to improve the accuracy and stability of the solution. Second-/third-stage separation occurs when the scramjet has expended all of its fuel. The third stage is then optimized for maximum payload from the calculated second-/third-stage separation point.

To ensure an optimal solution, the number of nodes that DIDO uses is manually varied between 96 and 105, and a solution is computed for each node value to ensure a distinct local minima. Ten solutions are observed to provide a sufficient number of node variations, with the solutions converging to similar local minima. The range of node values is chosen to produce accurate solutions, with efficient computation times. The final solution chosen corresponds to the node value that most minimizes the cost function, and thus minimizes the deviation from the 50 kPa dynamic pressure trajectory.

3. Second-Stage Optimization: Maximized Payload

For the maximum payload optimization, the second and third stages are considered using a dynamic programming approach. First, in order to increase the computational efficiency of the optimization, optimal third-stage payloads are tabulated over a 3 deg grid of separation conditions $\mathbf{x}_2(t_{2,f})$, as described in Sec. IV.B.1, providing the optimal payload for a range of velocity, altitude, and flight-path angles at separation, as shown in Fig. 7. Then, the interpolated third-stage payload is used as the terminal cost $C_{2 \rightarrow 3}(\mathbf{x}_2(t_{2,f}))$ for the calculation of the second-stage trajectory optimization, which optimizes both the second and third stages by setting the cost function to the maximize payload:

$$\min_{u_2} C_2(\mathbf{x}_2(t_2), \mathbf{u}_2(t_2)) + C_{2 \rightarrow 3}(\mathbf{x}_2(t_{2,f})) \quad (21)$$

where

$$C_2(\mathbf{x}_2(t_2), \mathbf{u}_2(t_2)) = 0.01 \int_{t_{2,0}}^{t_{2,f}} \dot{m}_{\text{fuel}} dt \quad (22)$$

$$C_{2 \rightarrow 3}(\mathbf{x}_2(t_{2,f})) = -m_{\text{payload}} \quad (23)$$

$C_2(\mathbf{x}_2(t_2), \mathbf{u}_2(t_2))$ is included to improve numerical stability and is weighted by a constant of 0.01 in order to have a negligible effect on the resultant trajectory. This problem is solved using the pseudospectral method [54]. As with the constant-dynamic-pressure case, the number of nodes is manually varied between 96 and 105, and a solution is computed for each node value, converging to similar local minima. The final solution chosen corresponds to the node value that most maximizes the payload to orbit of the vehicle. The third stage is optimized for the maximum payload from the calculated second-/third-stage separation point as a check to ensure that the interpolation provides an accurate payload-to-orbit result.

4. First-Stage Optimization

After launch, the first stage flies vertically to a 100 m altitude, when a pitchover is initiated. From pitchover, the first stage is optimized for the minimum fuel mass necessary to reach the first-/second-stage separation conditions $\mathbf{x}_1(t_{1,f})$ of 1520 m/s velocity, and the altitude and flight-path angle are determined by the second-stage trajectory.

The separation velocity of 1520 m/s corresponds to Mach 5.1 at 50 kPa, which is the minimum operating point of the proposed scramjet [5]. Release at the minimum operable point is advantageous because the scramjet specific impulse increases at low velocities [5].

The altitude and flight-path angle at first-/second-stage separation is defined by the optimized second stage. This approach is used on account of the selected first stage being able to reach the required range of altitudes and flight angles at 1520 m/s with small fuel mass variations. Nevertheless, a small variation in fuel mass can have an important effect on the capabilities of the first stage, influencing the velocity achievable at first- to second-stage separation, as well as the rate at which the rocket is able to pitch and, consequentially, the altitude and flight-path angle range of the first stage. The optimal (lowest fuel consumption) trajectory for the first-stage stack that can reach the first-/second-stage separation condition $\mathbf{x}_1(t_{1,f})$ is found by setting a cost function to minimize the fuel mass:

$$\min_{u_1} C_{1 \rightarrow 2}(\mathbf{x}_1(t_{1,f})) \quad (24)$$

where

$$C_{1 \rightarrow 2}(\mathbf{x}_1(t_{1,f})) = m_{\text{fuel}} \quad (25)$$

and the end point is fixed by the optimal second-stage start conditions. The first stage is limited to a -5° deg angle of attack to produce a conservative trajectory solution, which is within the capabilities of the vehicle. The optimal trajectory is determined using the pseudospectral method. Ten results are obtained by varying the number of nodes in DIDO between 90 and 99, converging to very similar minima. The final result is chosen as the solution that uses the least fuel.

V. Results and Discussion

LODESTAR is used to investigate the suitability of a pseudospectral method approach to optimization of scramjet–rocket trajectories and to develop optimal trajectory solutions. The following trajectories are developed:

- 1) The first trajectory is the $q = 50$ kPa fixed SPARTAN trajectory with minimum pullup. It verifies the simulation and provides a baseline trajectory.
- 2) The second trajectory is optimized for payload to orbit at $q_{\text{max}} = 50$ kPa. It demonstrates improved performance through coupled trajectory optimization.
- 3) The third trajectory is optimized for payload to orbit, with $q_{\text{max}} = 45$ kPa and $q_{\text{max}} = 55$ kPa. A comparison of these simulations allows investigation into the effect of the q maximum on the payload to orbit.
- 4) The fourth trajectory is optimized for payload to orbit, with $q_{\text{max}} = 50$ kPa and 110% SPARTAN drag. A comparison of optimal trajectories at 100 and 110% drag allows investigation of the robustness of the solution with variation in the vehicle design.

Table 1 details the key results for comparison.

A. First-Stage Evaluation: q Equal to Fifty-Kilopascal Second-Stage Separation

Figure 8 shows an example first-stage trajectory, optimized for minimum mass, with end conditions of 24.4 km altitude and a

1.56 deg flight-path angle. These separation conditions correspond to the second-stage separation conditions for a 50 kPa dynamic pressure trajectory.

The first stage flies a fixed vertical trajectory for 3.79 s; after which, a pitchover is initiated. After pitchover, the angle of attack reduces to -1.17° deg at 13.1 s. The angle of attack is then raised to 0.88° deg at 29.9 s before reducing gradually to the minimum of -5° deg, adjusting in stages in order to reach the desired end conditions. An altitude of 24.4 km is reached after a total flight time of 93.6 s, with a total ground distance of 34.5 km covered. This trajectory shape is very similar for all first-stage simulation cases.

B. Second-Stage Evaluation

1. Fixed Dynamic Pressure Trajectory, Minimum Pullup

A constant-dynamic-pressure trajectory with a pullup to a 1.5 deg flight-path angle at third-stage release is produced as a baseline for comparison with a payload-optimized trajectory, as well as to verify that LODESTAR is able to optimize a complex airbreathing trajectory. A pullup to a 1.5 deg flight-path angle is the minimum necessary for the third stage to reach orbit. At release angles below 1.5 deg, the thrust vector limitations necessary to produce a trimmed trajectory constrain the angle of attack of the third stage so that the rocket does not generate the lift required to exit the atmosphere. This angle-of-attack limitation, imposed by the maximum thrust vector, necessitates a scramjet-stage pullup maneuver in order for the third-stage rocket to operate successfully.

The constant-dynamic-pressure minimum pullup trajectory for the SPARTAN stage is shown in Figs. 9–11, with key results summarized in Table 1. Due to the clear objective of a constant-dynamic-pressure trajectory, any deviations from the target dynamic pressure are readily apparent, allowing the efficacy of the optimizer to be verified. These results show very close adherence to a 50 kPa dynamic pressure (maximum 0.29% deviation) until pullup at 336.4 s. Third-stage release occurs at 349.1 s at a 33.17 km altitude. Over the trajectory, the Mach number increases from 5.10 to 9.52 and the velocity from 1520 to 2905 m/s. The flap deflection shows an overall increase from -0.53 to 5.76° deg over the trajectory. The net specific impulse ($I_{\text{sp,net}} = (T - D)/\dot{m}g$) generally decreases over the trajectory as the efficiency of the scramjet engines decreases. However, at the beginning of the trajectory, the equivalence ratio increases as the capture limitations are relaxed with increasing Mach number. This causes the net specific impulse to increase to a maximum of 1739 s during the first 19.45 s of flight time.

Figure 20 shows the corresponding third-stage atmospheric exit trajectory after release, evaluated as described in Sec. II.C. After atmospheric exit, this trajectory is followed by a Hohmann transfer to a heliosynchronous orbit, resulting in a total payload to orbit of 156.8 kg.

2. Dynamic Pressure Limited Trajectory

LODESTAR is configured to optimize the total payload mass to orbit. A maximum dynamic pressure limit of 50 kPa is applied to the optimization process to allow direct comparison with the constant q trajectory and so that an equivalent vehicle can be used.

Table 1 Summary of simulation results

Trajectory condition	1) $q = 50$ kPa, $\gamma_{2 \rightarrow 3} = 1.5^\circ$ deg	2) $q \leq 50$ kPa, maximum m_{Payload}	3a) $q \leq 45$ kPa, maximum m_{Payload}	3b) $q \leq 55$ kPa, maximum m_{Payload}	4) $q \leq 50$ kPa, maximum m_{Payload} , 110% C_D
Payload to orbit, kg	156.8	169.9	163.9	176.4	161.8
Separation altitude; 1 \rightarrow 2, km	24.4	25.0	25.6	24.0	25.3
First-stage structural mass fraction	0.0740	0.0740	0.0744	0.0744	0.0749
Separation altitude; 2 \rightarrow 3, km	33.17	34.49	34.46	34.58	34.29
Separation v ; 2 \rightarrow 3, m/s	2905	2881	2861	2893	2829
Separation γ ; 2 \rightarrow 3, deg	1.50	2.91	2.31	3.39	2.97
Separation q ; 2 \rightarrow 3, kPa	46.3	36.9	36.59	36.71	36.7
Second-stage L/D; 2 \rightarrow 3	3.21	3.24	3.35	3.34	2.94
Second-stage flight time, s	349.1	357.0	381.8	326.8	356.9
Third-stage t ; $q > 20$ kPa, s	65	29	25	23	27

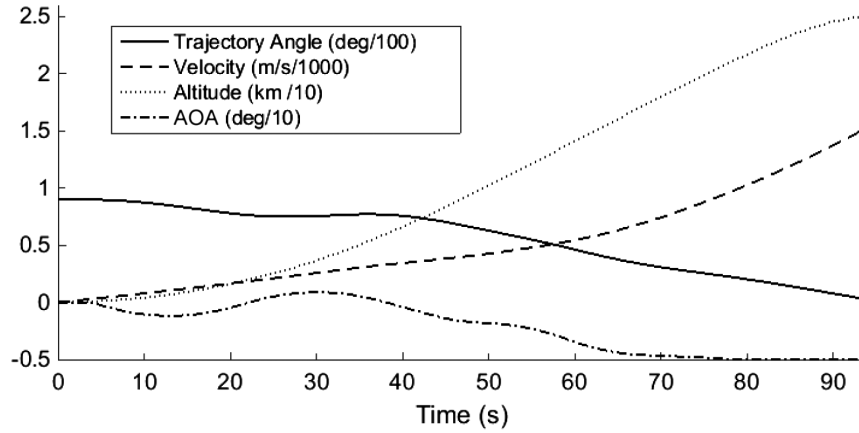


Fig. 8 First-stage trajectory, optimized for minimum fuel mass and a release point of 50 kPa.

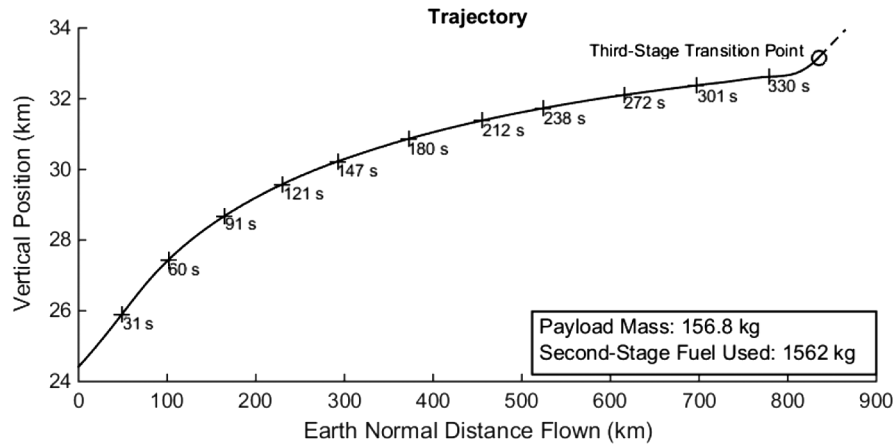


Fig. 9 Trajectory path of the second-stage SPARTAN vehicle flying at 50 kPa constant dynamic pressure, with 1.5 deg third-stage release angle.

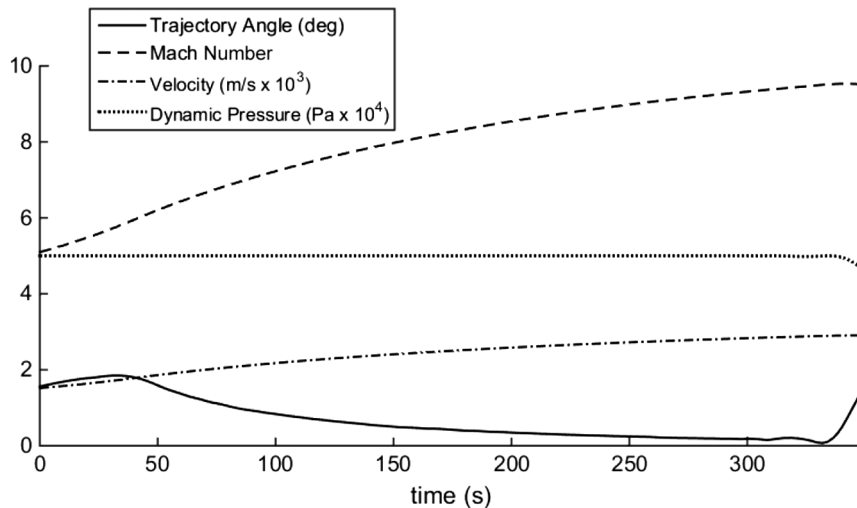


Fig. 10 Trajectory data for 50 kPa constant-dynamic-pressure trajectory, with 1.5 deg third-stage release angle.

The optimal trajectory shape for a $q = 50$ kPa limited, maximum payload to orbit trajectory is shown in Figs. 12–14, with key results summarized in Table 1. The equivalence ratio of the engine is less than one until 52.77 s, causing the SPARTAN to fly under 50 kPa in this region (to a minimum of 40.8 kPa) in order to raise the equivalence ratio by flying in a higher-temperature region. This increase in equivalence ratio results in a corresponding increase in net specific impulse. After the equivalence ratio increases to one, the trajectory follows a constant-dynamic-pressure path at 50 kPa until

331.7 s; at which point, a pullup maneuver is performed, gaining altitude until rocket-stage release at a 357.0 s flight time. This trajectory is able to deliver 169.9 kg of payload to heliocentric orbit, which is an increase of 8.35% over the constant-dynamic-pressure result with minimum pullup. The point at which the pullup maneuver begins is the optimization result that takes into account the best combination of velocity, altitude, and release angle for scramjet-stage performance and the release of the rocket stage. This pullup indicates the region at which the increasing altitude and release angle become

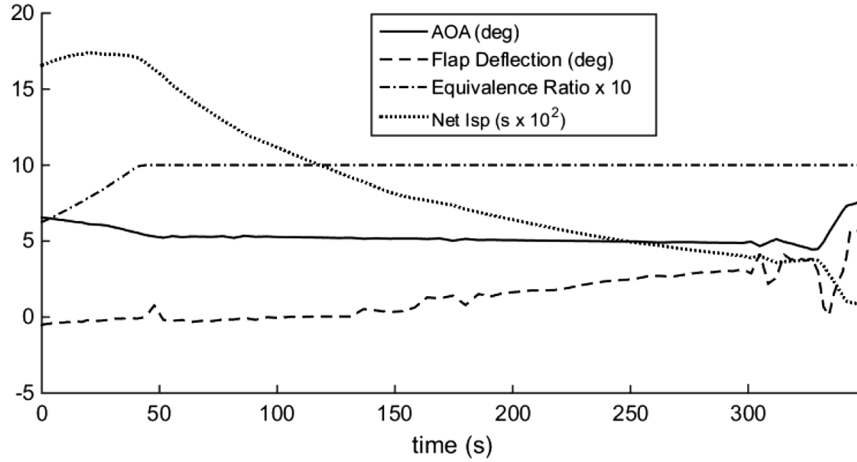


Fig. 11 Vehicle performance data for 50 kPa constant-dynamic-pressure trajectory, with 1.5 deg third-stage release angle. Note that flap deflection is positive down.

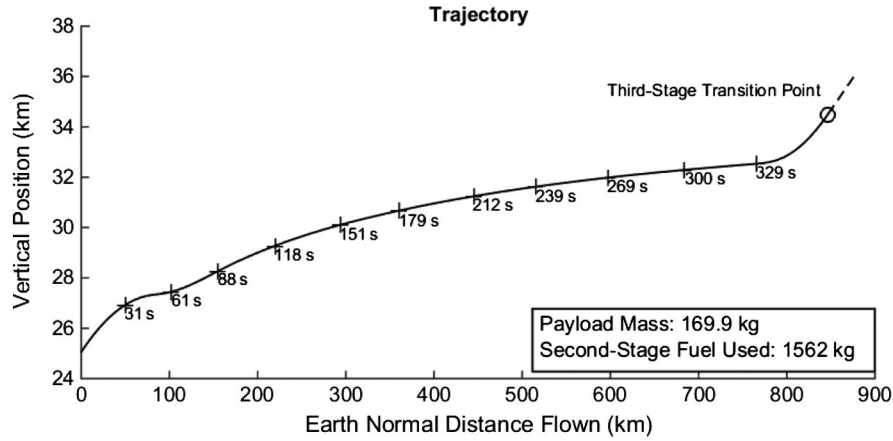


Fig. 12 Maximum payload trajectory path of the second-stage SPARTAN vehicle when limited to a 50 kPa dynamic pressure.

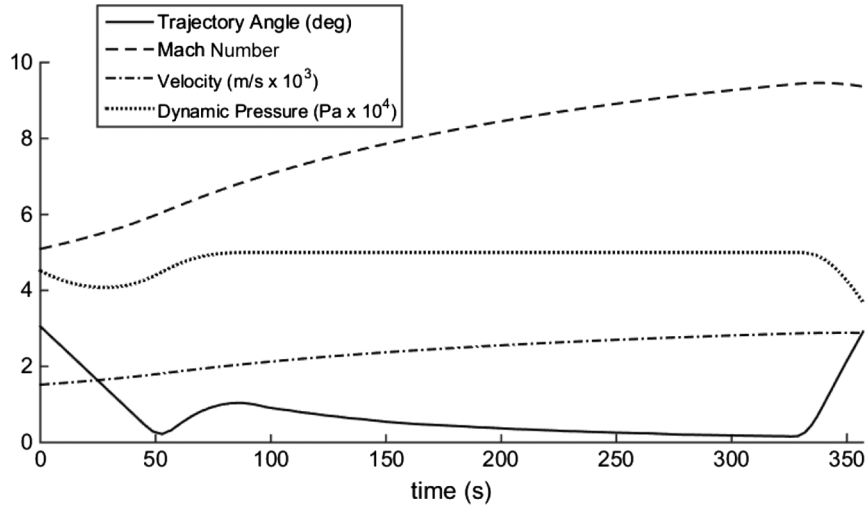


Fig. 13 Trajectory data for a 50 kPa dynamic pressure limited trajectory.

more important than extracting the maximum thrust from the scramjet (which is attained at high q and a low flight angle at an equivalence ratio of one). Flight in a lower-dynamic-pressure environment results in less thrust output from the scramjet engines, as well as an increase in the angle of attack and flap deflection angle to compensate for the additional lift required. Due to this, less overall acceleration is obtained as compared to the constant-dynamic-pressure result with minimum pullup. Separation occurs at a velocity

of 2881 m/s, which is a decrease of 24 m/s. However, at the same time separation altitude, it increases by 1.32 to 34.49 km, resulting in a decrease in the separation dynamic pressure to 36.9 kPa.

The larger scramjet-stage pullup assists the rocket in maneuvering to an exoatmospheric altitude by increasing the altitude and angle at separation by virtue of the increased L/D ratio and maneuverability of the scramjet vehicle. Even a small increase in release angle, to the optimal angle of 2.91 deg, significantly reduces the turning that is

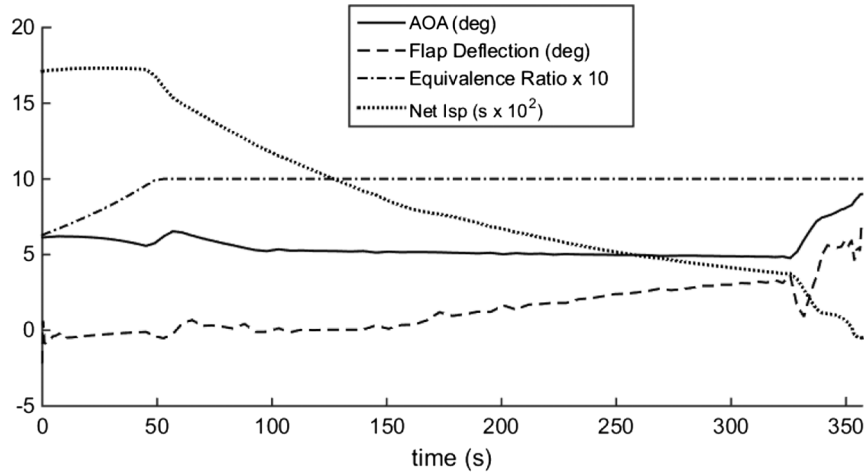


Fig. 14 Vehicle performance data for a 50 kPa dynamic pressure limited trajectory. Note that flap deflection is positive down.

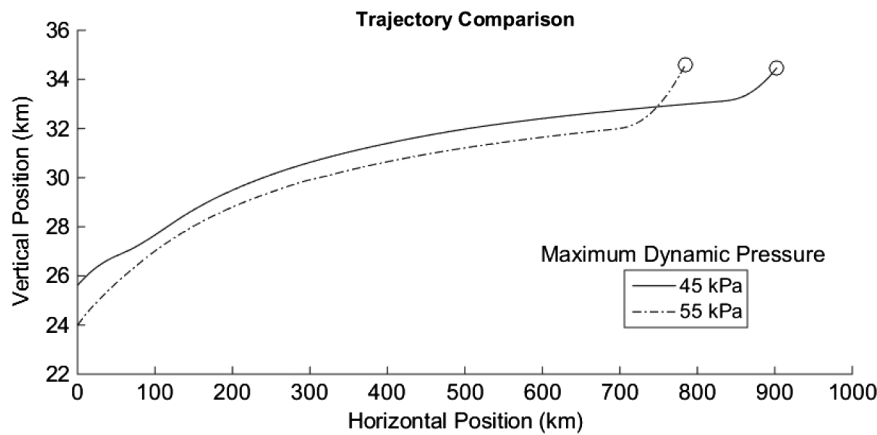


Fig. 15 Comparison of 45/55 kPa dynamic pressure limited trajectory paths for the maximum payload to orbit.

required by the rocket, as is evident from comparing Figs. 20 and 21. Further benefits are the reduced time that the rocket must spend in a high-dynamic-pressure environment and a decrease in the maximum dynamic pressure that the rocket stage experiences by 20.3%, as shown in Table 1. This allows the structural mass and heat shielding, which are necessary to achieve exoatmospheric flight, to be decreased, enabling higher payload to orbit.

Compared to studies considering vehicles with a scramjet–rocket transition within a single stage [10,11], the maximum payload-to-orbit trajectory of the multistage system shows a scramjet–rocket transition point at much lower altitudes. This lower transition point is a consequence of the stage separation creating an energy tradeoff, which does not occur in a single-stage vehicle. Single-stage vehicles must necessarily transport all components to the exoatmosphere, and so use the scramjet engines until a higher altitude to take advantage of their high efficiency. A multistage vehicle is able to separate the scramjet stage. This separation occurs when the performance benefits provided by the superior aerodynamics and engine efficiency of the scramjet stage are offset by the energy required to lift the extra mass to a higher altitude. The beneficial ability to separate the scramjet-stage results in a lower-altitude scramjet–rocket transition point when compared to single-stage vehicle designs.

3. Dynamic Pressure Sensitivity

To investigate the sensitivity of the vehicle to changes in q_{\max} , the maximum dynamic pressure is varied to 45 and 55 kPa and the flight trajectory optimized, with results shown in Figs. 15–17 and summarized in Table 1. The $\pm 10\%$ variation in maximum dynamic pressure has very little effect on the payload mass delivered to heliocentric orbit. Varying the maximum dynamic pressure by ± 5 kPa from 50 kPa causes a variation of only +6.5 kg (+3.8%) or

–6.0 kg (–3.5%) in the payload to orbit. Separation altitudes of 34.46 and 34.58 km are reached for 45 and 55 kPa limited cases, respectively, with separation velocities of 2861 and 2893 m/s. The 45 kPa limited case flies for 381.8 s, which is significantly longer than the 55 kPa case that flies for 326.8 s. Both trajectories pull up to similar altitudes, with relatively small variation in separation velocity (–20 or +12 m/s). This small variation in velocity is despite the increase in air density and decrease in angle of attack required for flight at a 55 kPa dynamic pressure, both of which increase the mass flow into the engine. Although the thrust output of the REST engines increases with dynamic pressure, so does the drag on the vehicle; and the net increase in performance is small.

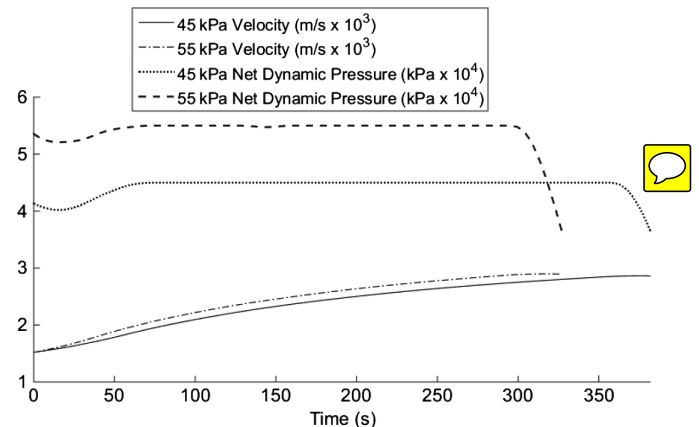


Fig. 16 Comparison of trajectory data for 45/55 kPa dynamic pressure limited trajectories.

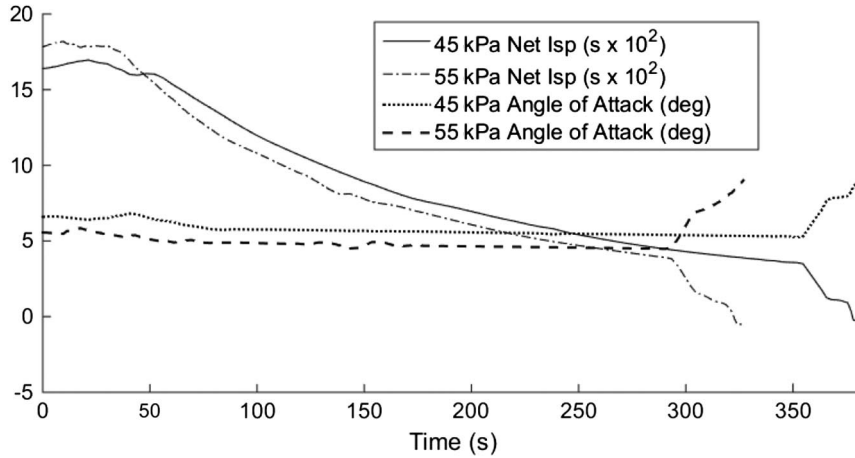


Fig. 17 Comparison of vehicle performance data for 45/55 kPa dynamic pressure limited trajectories.

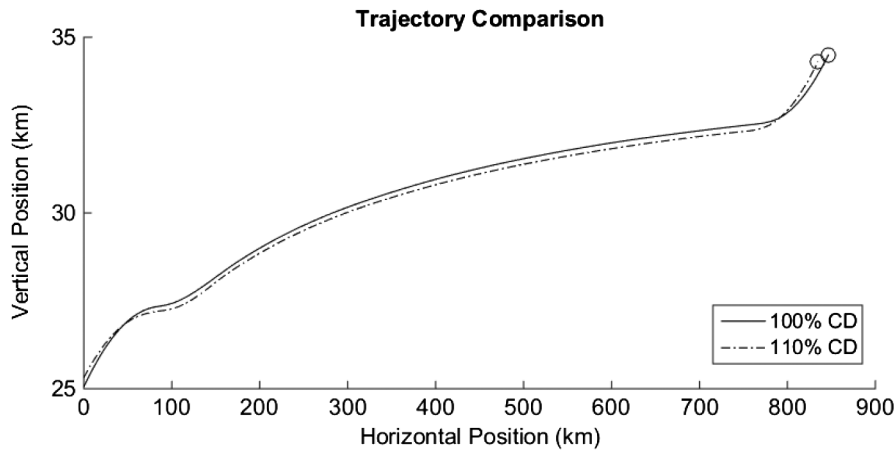


Fig. 18 Comparison of trajectory paths for 100 and 110% drag cases for a 50 kPa dynamic pressure limited maximum payload trajectory.

Only a small variation in optimal payload mass is observed, without modification of vehicle design, to account for the dynamic pressure limit. This indicates that designing and operating a vehicle at lower dynamic pressures may be preferable. Flying at a lower maximum dynamic pressure allows reduction of the structural weight and heat shielding of the vehicle. However, as the 45 kPa limited case has a higher first-/second-stage separation altitude, a larger first-stage fuel mass is required, although this increase in fuel mass is small. Between 25.6 and 24.0 km (45 and 55 kPa optimal start points), there is only a 2.2% variation in the fuel mass required. This small variation in first-stage fuel consumption would easily be offset by a decrease in second-stage structural mass.

4. Drag Sensitivity Analysis

To investigate the effect of vehicle design and uncertainty in aerodynamic performance on the optimal trajectory, the drag on the vehicle is increased by 10%, and an optimized trajectory calculated with dynamic pressure is limited to 50 kPa. Selected results are compared to the 100% drag results in Figs. 18 and 19. These results show that, when drag is increased (i.e., L/D is decreased), the optimal trajectory shape is similar to the baseline case, although the high drag second stage follows a slightly slower, and hence lower, flight path with a lower-stage transition point. The similar flight-path shape of the high drag case suggests that sacrificing velocity to increase separation altitude in a pullup maneuver is optimal for multiple vehicle designs. However, the lower transition point indicates that the rocket is favored at an earlier point in the climb maneuver due to the decreased aerodynamic efficiency of the scramjet vehicle. The net result is a lower payload to orbit of 161.8 kg (a decrease of 4.8%).

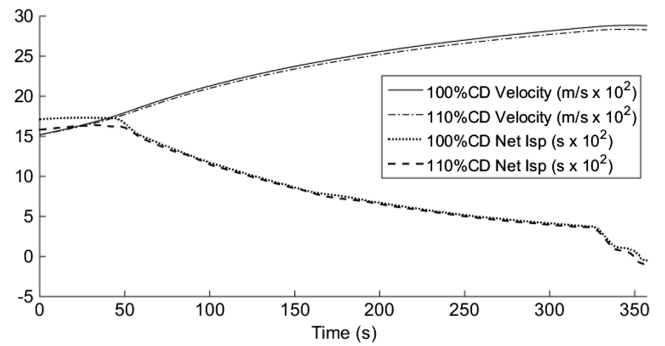


Fig. 19 Comparison of v and $I_{sp,net}$ for 100 and 110% drag cases for a 50 kPa dynamic pressure limited maximum payload trajectory.

C. Third-Stage Evaluation

Third-stage trajectories for release angles of 1.50 and 2.91 deg are shown in Figs. 20 and 21. These trajectories correspond to third-stage release points at the end of a constant-dynamic-pressure trajectory with minimum pullup (as shown in Sec. V.B.1) and an optimized 50 kPa limited trajectory (as shown in Sec. V.B.2). These third-stage trajectories show a pullup to high altitude before the circularization burn is performed.

The third stage released at 1.5 deg, shown in Fig. 20, is limited by the maximum thrust vector angle for the first 47 s of flight. This places significant limitations on the maximum allowable angle of attack. This angle-of-attack limitation reduces the lift of the rocket, causing it to spend a large amount of time at low altitude, in a high drag

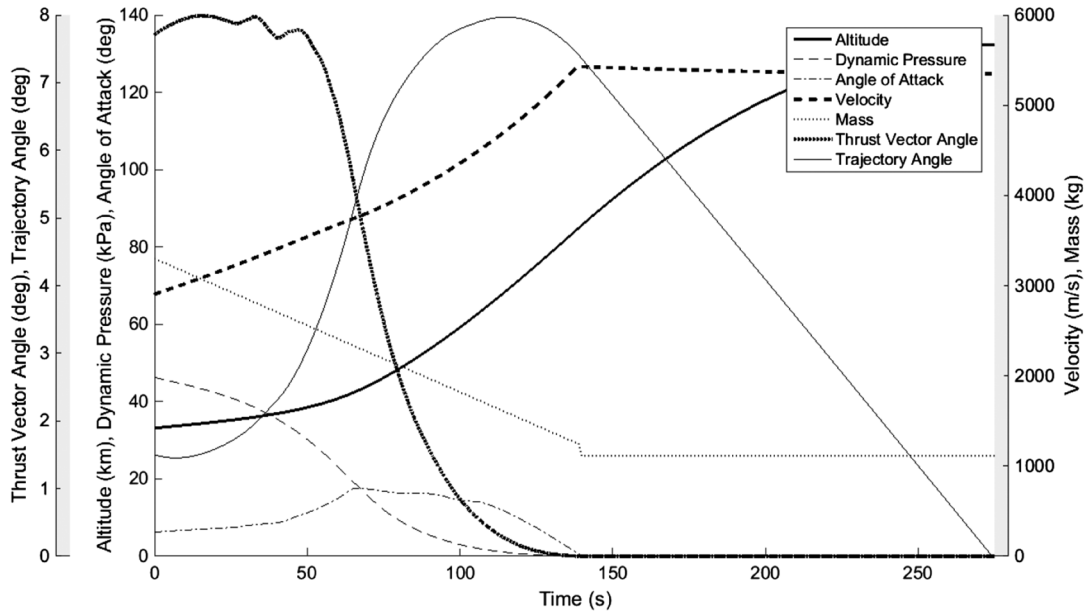


Fig. 20 Third-stage rocket trajectory simulated from the end of the 50 kPa constant-dynamic-pressure SPARTAN trajectory, released at an angle of 1.50 deg, with a velocity of 2905 m/s and an altitude of 33.17 km.

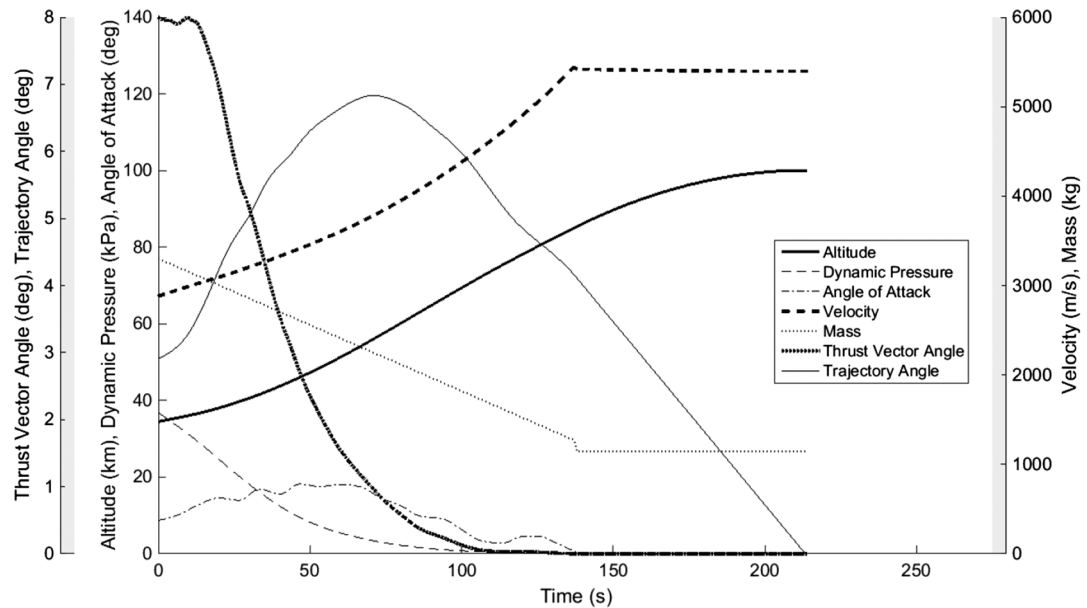


Fig. 21 Third-stage rocket trajectory simulated from the end of the 50 kPa dynamic pressure limited maximum payload SPARTAN trajectory, released at an angle of 2.91 deg, a velocity of 2881 m/s, and an altitude of 34.49 km.

environment. The angle of attack increases gradually to a maximum of 17.6 deg at 66 s before decreasing until burnout at 140 s.

The release of the third-stage rocket from an optimized scramjet trajectory is shown in Fig. 21. Release at a higher, more optimal angle mitigates the effects of the thrust vector angle limitation so that the thrust vector limit is only reached during the first 10 s of flight time. After this, the angle of attack is limited by the maximum allowable normal force rather than the thrust vector limit, resulting in a higher maximum angle of attack. The rocket increases the flight-path angle and gains altitude rapidly, resulting in less time spent in a high drag environment and a larger payload to orbit. The angle of attack is increased gradually to 18.14 deg at 48 s before decreasing until burnout at 138 s.

VI. Conclusions

In this paper, the optimal control program LODESTAR is used to design the trajectory of a rocket–scramjet–rocket multistage system.

This system consists of a rocket-powered first stage modeled on a scaled down LOX–kerosene SpaceX Falcon-1e; the SPARTAN, which is a scramjet accelerator being developed at the University of Queensland; and a LOX–kerosene rocket-powered third stage based on the SpaceX Kestrel engine. Applied to full trajectory optimization, LODESTAR is able to generate optimized trajectories that increase the payload to orbit of the multistage system.

When flying at a constant 50 kPa dynamic pressure, the results indicate that a scramjet-stage pullup, to a minimum of a 1.50 deg flight-path angle, is necessary in order for the third-stage rocket to reach orbit successfully. Trajectory optimization for maximum payload indicates that the optimal scramjet flight path for a system transitioning between separate airbreathing and rocket-powered stages is to fly at lower than maximum dynamic pressure while the equivalence ratio is less than one, followed by constant-dynamic-pressure flight at maximum dynamic pressure, and finally a pullup maneuver. The optimal pullup maneuver trades off velocity (a decrease of 24 m/s) for altitude (an increase of 1.32 km) and improved flight-path angle (an increase of

1.41 deg) when compared to the minimum pullup case. The optimal flight path increases payload mass to heliocentric orbit by 13.1 kg (8.35%) as compared to a constant-dynamic-pressure trajectory with minimum necessary pullup. The larger pullup maneuver in the payload-optimized trajectory also reduces the third-stage dynamic pressure to 36.9 kPa, which is a decrease of 20.3% as compared to a trajectory with minimum pullup. This decrease in maximum dynamic pressure decreases the stress experienced by the rocket stage proportionally, as well as decreasing the heat flux into the rocket: both of which lead to significant benefits for the design of the rocket stage (which are not taken into account in this study). A decrease in structural stress allows for less internal reinforcement, and a decrease in heat flux allows for reduction of the heat shield size, potentially resulting in further increases in payload mass.

As part of a dynamic pressure sensitivity evaluation, the maximum dynamic pressure limit of the SPARTAN vehicle is varied by ± 5 kPa. This produces only +3.8% and -3.5% variations on the payload mass delivered to orbit. This small variation in the payload to orbit indicates that a scramjet-powered stage designed for operation at lower dynamic pressure may be advantageous. If efficient, low-dynamic-pressure scramjet engines are available; operating at lower dynamic pressure enables lighter vehicles due to reduced structural and thermal loads. This reduction in mass potentially leads to further performance improvements and operational benefits, including an increased payload to orbit and extended range.

To investigate the effect of changes in second-stage vehicle properties, the drag of the scramjet was increased by 10% and the optimal trajectory evaluated. This resulted in a pullup maneuver with a lower second-/third-stage transition point when compared to the original result. This variation in the optimal trajectory was minor, indicating that the presented trajectory shape was robust with respect to changes in vehicle design and, by extension, changes in engine performance or vehicle aerodynamics. Overall, this work provided new insight into the preferred operating ranges for scramjet vehicles incorporated in multistage-to-orbit systems.

Acknowledgments

This research was supported in part by an Australian Government Research Training Program Scholarship. The authors would like to thank Dawid Preller for his work on the SPARTAN vehicle, which was integral to this study; and Joseph Chai for providing the CAD model of the SPARTAN.

References

- [1] 2015 Commercial Space Transportation Forecasts, Federal Aviation Administration Office of Commercial Space Transportation, and the Commercial Space Transportation Advisory Committee, Washington, D.C., May 2015.
- [2] Smart, M. K., and Tetlow, M. R., "Orbital Delivery of Small Payloads Using Hypersonic Airbreathing Propulsion," *Journal of Spacecraft and Rockets*, Vol. 46, No. 1, 2009, pp. 117–125. doi:10.2514/1.38784
- [3] Heiser, H. H., and Pratt, D. T., *Hypersonic Airbreathing Propulsion*, AIAA, Washington, D.C., 1994. doi:10.2514/4.470356
- [4] Flaherty, K. W., Andrews, K. M., and Liston, G. W., "Operability Benefits of Airbreathing Hypersonic Propulsion for Flexible Access to Space," *Journal of Spacecraft and Rockets*, Vol. 47, No. 2, 2010, pp. 280–287. doi:10.2514/1.43750
- [5] Preller, D., and Smart, M. K., "Reusable Launch of Small Satellites Using Scramjets," *Journal of Spacecraft and Rockets*, Vol. 54, No. 6, 2017, pp. 1317–1329. doi:10.2514/1.A33610
- [6] Kimura, T., and Sawada, K., "Three-Stage Launch System with Scramjets," *Journal of Spacecraft and Rockets*, Vol. 36, No. 5, 1999, pp. 675–680. doi:10.2514/2.3500
- [7] Olds, J., and Budianto, I., "Constant Dynamic Pressure Trajectory Simulation with POST," *Aerospace Sciences Meeting and Exhibit*, AIAA Paper 1998-0302, 1998, pp. 1–13. doi:10.2514/6.1998-302
- [8] "Falcon 1 Launch Vehicle Payload User's Guide," Space Exploration Technologies TR, Hawthorne, CA, 2008.
- [9] Powell, R. W., Shaughnessy, J. D., Cruz, C. I., and Naftel, J. C., "Ascent Performance of an Air-Breathing Horizontal-Takeoff Launch Vehicle," *Journal of Guidance, Control, and Dynamics*, Vol. 14, No. 4, 1991, pp. 834–839. doi:10.2514/3.20719
- [10] Lu, P., "Inverse Dynamics Approach to Trajectory Optimization for an Aerospace Plane," *Journal of Guidance, Control, and Dynamics*, Vol. 16, No. 4, 1993, pp. 726–732. doi:10.2514/3.21073
- [11] Trefny, C., "An Air-Breathing Concept Launch Vehicle for Single-Stage-to-Orbit," *35th Joint Propulsion Conference and Exhibit*, AIAA Paper 1999-2730, 1999. doi:10.2514/6.1999-2730
- [12] Roche, J. M., and Kosareo, D. N., "Structural Sizing of a 25000-Lb Payload, Air-Breathing Launch Vehicle for Single-Stage-to-Orbit," TR 2001, Jan. 2000.
- [13] Pescetelli, F., Minisci, E., Maddock, C., Taylor, I., and Brown, R., "Ascent Trajectory Optimisation for a Single-Stage-to-Orbit Vehicle with Hybrid Propulsion," *18th AIAA/3AF International Space Planes and Hypersonic Systems and Technologies Conference*, AIAA Paper 2012-5828, 2012, pp. 1–18. doi:10.2514/6.2012-5828
- [14] Young, D., Kokan, T., Tanner, C., Clark, I., Tanner, C., and Wilhite, A., "Lazarus: A SSTO Hypersonic Vehicle Concept Utilizing RBCC and HEDM Propulsion Technologies," *14th AIAA/AHI Space Planes and Hypersonic Systems and Technologies Conference*, AIAA Paper 2006-8099, 2006, pp. 1–15. doi:10.2514/6.2006-8099
- [15] Bradford, J., Olds, J., Bechtel, R., Cormier, T., and Messitt, D., "Exploration of the Design Space for the ABLV-GT SSTO Reusable Launch Vehicle," *Space 2000 Conference and Exposition*, AIAA Paper 2000-5136, Sept. 2000. doi:10.2514/6.2000-5136
- [16] Tsuchiya, T., and Mori, T., "Optimal Design of Two-Stage-to-Orbit Space Planes with Airbreathing Engines," *Journal of Spacecraft and Rockets*, Vol. 42, No. 1, 2005, pp. 90–97. doi:10.2514/1.8012
- [17] Wilhite, A. W., Engelund, W. C., Stanley, D. O., and Naftel, J. C., "Technology and Staging Effects on Two-Stage-to-Orbit Systems," *Journal of Spacecraft and Rockets*, Vol. 31, No. 1, 1994, pp. 31–38. doi:10.2514/3.26399
- [18] Mehta, U. B., and Bowles, J. V., "Two-Stage-to-Orbit Spaceplane Concept with Growth Potential," *Journal of Propulsion and Power*, Vol. 17, No. 6, 2001, pp. 1149–1161. doi:10.2514/2.5886
- [19] Bedrossian, N., Technologies, B., and Nasa, L. N., "Zero Propellant Maneuver Flight Results for 180 deg ISS Rotation," *20th International Symposium on Space Flight Dynamics*, Annapolis, MD, 2007.
- [20] Josselyn, S., and Ross, I. M., "Rapid Verification Method for the Trajectory Optimization of Reentry Vehicles," *Journal of Guidance, Control, and Dynamics*, Vol. 26, No. 3, 2003, pp. 505–508. doi:10.2514/2.5074
- [21] Yang, S., Cui, T., Hao, X., and Yu, D., "Trajectory Optimization for a Ramjet-Powered Vehicle in Ascent Phase via the Gauss Pseudospectral Method," *Aerospace Science and Technology*, Vol. 67, Aug. 2017, pp. 88–95. doi:10.1016/j.ast.2017.04.001
- [22] Rizvi, S. T. U. I., He, L. S., and Xu, D. J., "Optimal Trajectory and Heat Load Analysis of Different Shape Lifting Reentry Vehicles for Medium Range Application," *Defence Technology*, Vol. 11, No. 4, 2015, pp. 350–361. doi:10.1016/j.dt.2015.06.003
- [23] Chai, D., Fang, Y. W., Wu, Y. L., and Xu, S. H., "Boost-Skipping Trajectory Optimization for Air-Breathing Hypersonic Missile," *Aerospace Science and Technology*, Vol. 46, Oct.–Nov. 2015, pp. 506–513. doi:10.1016/j.ast.2015.09.004
- [24] Moshman, N. D., and Proulx, R. J., "Range Improvements in Gliding Reentry Vehicles from Thrust Capability," *Journal of Spacecraft and Rockets*, Vol. 51, No. 5, 2014, pp. 1681–1694. doi:10.2514/1.A32764
- [25] Rao, A. V., "A Survey of Numerical Methods for Optimal Control," *Advances in the Astronautical Sciences*, Vol. 135, American Astronomical Society, Washington, D.C., 2009, pp. 497–528, <http://vdo1.mae.ufl.edu/ConferencePublications/trajectorySurveyAAS.pdf> [retrieved 2018].

16



















- [26] Fahroo, F., and Ross, I., "Direct Trajectory Optimization by a Chebyshev Pseudospectral Method," *Proceedings of the 2000 American Control Conference*, Chicago, IL, 2000, pp. 3860–3864. doi:10.1109/ACC.2000.876945
- [27] Stryk, O., and Bulirsch, R., "Direct and Indirect Methods for Trajectory Optimization," *Annals of Operations Research*, Vol. 37, No. 1, 1992, pp. 357–373. doi:10.1007/BF02071065
- [28] Boggs, P., and Tolle, J., "Sequential Quadratic Programming for Large-Scale Nonlinear Optimization," *Journal of Computational and Applied Mathematics*, Vol. 124, Nos. 1–2, 2000, pp. 123–137. doi:10.1016/S0377-0427(00)00429-5
- [29] Elnagar, G., Kazemi, M. A., and Razzaghi, M., "The Pseudospectral Legendre Method for Discretizing Optimal Control Problems," *IEEE Transactions on Automatic Control*, Vol. 40, No. 10, 1995, pp. 1793–1796. doi:10.1109/9.467672
- [30] Garg, D., Patterson, M., and Hager, W., "An Overview of Three Pseudospectral Methods for the Numerical Solution of Optimal Control Problems," *Advances in the Astronautical Sciences*, Vol. 135, American Astronomical Society, Washington, D.C., 2009, Paper AAS 09-332, <http://vdol.mae.ufl.edu/ConferencePublications/unifiedFrameworkAAS.pdf> [retrieved 2018].
- [31] Fahroo, F., and Ross, I., "Computational Optimal Control by Spectral Collocation with Differential Inclusion," *1999 Flight Mechanics Symposium*, Greenbelt, MD, 1999, pp. 185–200.
- [32] Huntington, G. T., and Rao, A. V., "Optimal Reconfiguration of Spacecraft Formations Using the Gauss Pseudospectral Method," *Journal of Guidance, Control, and Dynamics*, Vol. 31, No. 3, 2008, pp. 689–698. doi:10.2514/1.31083
- [33] Yan, H., Ross, I. M., and Alfriend, K. T., "Pseudospectral Feedback Control for Three-Axis Magnetic Attitude Stabilization in Elliptic Orbits," *Journal of Guidance, Control, and Dynamics*, Vol. 30, No. 4, 2007, pp. 1107–1115. doi:10.2514/1.26591
- [34] Preller, D., and Smart, M. K., "Scramjets for Reusable Launch of Small Satellites," *20th AIAA International Space Planes and Hypersonic Systems and Technologies Conference*, AIAA Paper 2015-3586, 2015, pp. 1–23. doi:10.2514/6.2015-3586
- [35] Jazra, T., Preller, D., and Smart, M. K., "Design of an Airbreathing Second Stage for a Rocket-Scramjet-Rocket Launch Vehicle," *Journal of Spacecraft and Rockets*, Vol. 50, No. 2, 2013, pp. 411–422. doi:10.2514/1.A32381
- [36] Suraweera, M., and Smart, M. K., "Shock Tunnel Experiments with a Mach 12 {REST} Scramjet at Off-Design Conditions," *Journal of Propulsion and Power*, Vol. 25, No. 3, 2009, pp. 555–564. doi:10.2514/1.37946
- [37] Gollan, R. J., and Smart, M. K., "Design of Modular, Shape-Transitioning Inlets for a Conical Hypersonic Vehicle," *Aerospace, AIAA*, Vol. 29, No. 4, 2013, pp. 832–838. doi:10.2514/6.2010-940
- [38] Aftosmis, M. J., Berger, M. J., and Adomavicius, G., "A Parallel Multilevel Method for Adaptively Refined Cartesian Grids with Embedded Boundaries," *38th Aerospace Sciences Meeting and Exhibit*, AIAA Paper 2000-808, 2000. doi:10.2514/6.2000-808
- [39] Aftosmis, M. J., Berger, M. J., and Melton, J. E., "Robust and Efficient Cartesian Mesh Generation for Component-Based Geometry," *AIAA Journal*, Vol. 36, No. 6, 1998, pp. 952–960. doi:10.2514/2.464
- [40] Mehta, U., Aftosmis, M., Bowles, J., and Pandya, S., "Skylon Aerodynamics and SABRE Plumes," *20th AIAA International Space Planes and Hypersonic Systems and Technologies Conference*, AIAA Paper 2015-3605, 2015, pp. 1–21. doi:10.2514/6.2015-3605
- [41] Sagerman, D. G., Rumpfkeil, M. P., Hellman, B. M., and Dasque, N., "Comparisons of Measured and Modeled Aero-Thermal Distributions for Complex Hypersonic Configurations," *55th AIAA Aerospace Sciences Meeting*, AIAA Paper 2017-0264, Jan. 2017, pp. 1–22. doi:10.2514/6.2017-0264
- [42] Abeynayake, D., and Agon, A., "Comparison of Computational and Semi-Empirical Aerodynamics Tools for Making Fit-for-Purpose Modelling Decisions," *20th International Congress on Modelling and Simulation*, Adelaide, Australia, 2013, pp. 1–6.
- [43] Aftosmis, M. J., Nemec, M., and Cliff, S. E., "Adjoint-Based Low-Boom Design with Cart3D," *29th AIAA Applied Aerodynamics Conference 2011*, AIAA Paper 2011-3500, 2011, pp. 1–17. doi:10.2514/6.2011-3500
- [44] PTC, "www.ptc.com," 2017, <http://www.ptc.com/cad/creo/parametric>.
- [45] Pointwise, "www.pointwise.com," 2017, <http://www.pointwise.com/>.
- [46] Jazra, T., and Smart, M., "Development of an Aerodynamics Code for the Optimisation of Hypersonic Vehicles," *47th AIAA Aerospace Sciences Meeting Including the New Horizons Forum and Aerospace Exposition*, AIAA Paper 2009-1475, 2009. doi:10.2514/6.2009-1475
- [47] Rosema, C., Doyle, J., Auman, L., Underwood, M., and Blake, W. B., "Missile DATCOM User's Manual-2011 Revision," U.S. Army Aviation and Missile Research Development TR, 2011. doi:10.21236/ad1000581
- [48] Zandbergen, B., "Modern Liquid Propellant Rocket Engines, 2000 Outlook," Delft Univ. of Technology TR, Delft, The Netherlands, Oct. 2000. doi:10.13140/2.1.4640.0003
- [49] *U.S. Standard Atmosphere, 1976*, NASA, U.S. Government Printing Office, Washington, D.C., 1976, <http://ntrs.nasa.gov/archive/nasa/casi.ntrs.nasa.gov/19770009539.pdf>.
- [50] Sutton, G., and Biblarz, O., *Rocket Propulsion Elements*, 8th ed., Wiley, New York, 2010. doi:10.1017/S0001924000034308
- [51] Bertsekas, D. P., *Dynamic Programming and Optimal Control*, Vol. I, Athena Scientific, Belmont, MA, 2005.
- [52] Ross, I. M., *A Beginners Guide to DIDO (ver 7.3): A MATLAB Application Package for Solving Optimal Control Problems*, Elissar, LLC, Monterey, CA, 2015.
- [53] Diehl, M., Bock, H. G., Diedam, H., and Wieber, P. B., "Fast Direct Multiple Shooting Algorithms for Optimal Robot Control," *Fast Motions in Biomechanics and Robotics*, Vol. 340, Lecture Notes in Control and Information Sciences, Springer, New York, 2006, pp. 65–93.
- [54] Ross, I. M., and Fahroo, F., "Pseudospectral Knotting Methods for Solving Nonsmooth Optimal Control Problems," *Journal of Guidance, Control, and Dynamics*, Vol. 27, No. 3, 2004, pp. 397–405. doi:10.2514/1.3426
- [55] Gill, P. E., Murray, W., and Saunders, M. A., "SNOPT: An SQP Algorithm for Large-Scale Constrained Optimization," *SIAM Journal on Optimization*, Vol. 12, No. 4, 2002, pp. 979–1006. doi:10.1137/S1052623499350013
- [56] "MATLAB and Optimization Toolbox Release 2014b," MathWorks, Inc., Natick, MA, 2014.

R. Schwane
Associate Editor

18

19

Queries

1. AU: Please check that the copyright (©) type is correct. Please note that the code will be added upon publication. 
2. AU: Please define C-REST 
3. AU: CFD was defined as computational fluid dynamics. Please confirm this is correct. 
4. AU: Instructions from AIAA indicate that figures are to appear in color only online. Please verify the usage of color in your proof is correct, and note that all figures will be grayscale in the print journal. We strongly suggest differentiating the items in color with symbols or other means for clarity in the print journal. 
5. AU: Please clarify/define HYPAERO. 
6. AU: Please define DATCOM if it is an acronym. 
7. AU: The numbered items were edited to be complete sentences, per journal guidelines. Please confirm your meaning was retained. 
8. AU: Please clarify the meanings of the numbers/bullets in Table 1. 
9. AU: As AIAA requires a 0 (zero) be inserted before a decimal point for numbers less than 1, please check that all values are correct. 
10. AU: As AIAA requires the figures to be cited in the order in which they appear in the main text, please reorder and renumber the figures accordingly. 
11. AU: Please note that AIAA requires financial support be listed first in the Acknowledgments. 
12. AU: Please provide the report numbers for Refs. [1, 8, 47, 48]. 
13. AU: If citing specific pages from Refs. [3, 50–52], please provide them. 
14. AU: For Ref. [12], please provide the name and location of the institution. 
15. AU: If Ref. [19] is a published proceedings, please provide the full name and location of the publisher (NOT of the conference host) and the page range. If it is a conference paper, please provide the paper number and the organizer's name. 
16. AU: For Refs. [26, 31, 42], please provide the full names and location of the publishers (NOT the conference hosts). 
17. AU: Please note that some of the urls were removed because they are no longer valid. If you would like to provide valid urls, please also provide the date of retrieval. 
18. AU: For Refs. [44, 45], please clarify the type of references listed. If they are databases, please add "[online database]". If you are only citing Web sites, please change to footnotes. Please also note that only one url may appear in each reference, and all urls require a date of retrieval. 
19. AU: The url was removed from Ref. [56], as urls must take the reader directly to the listed reference. If you would like to provide an accurate url, please also provide the date of retrieval. 